

## SUBMILLIMETER ARRAY 440 $\mu$ M/690GHZ LINE AND CONTINUUM OBSERVATIONS OF ORION-KL

H. BEUTHER<sup>1</sup>, Q. ZHANG<sup>1</sup>, M.J. REID<sup>1</sup>, T.R. HUNTER<sup>1</sup>, M. GURWELL<sup>1</sup>, D. WILNER<sup>1</sup>,  
 J.-H. ZHAO<sup>1</sup>, H. SHINNAGA<sup>1</sup>, E. KETO<sup>1</sup>, P.T.P. HO<sup>1</sup>, J.M. MORAN<sup>1</sup>, S.-Y. LIU<sup>2</sup>  
 hbeuther@cfa.harvard.edu

*Draft from February 5, 2008, submitted to ApJ*

### ABSTRACT

Submillimeter Array observations of Orion-KL at  $\sim 1''$  resolution in the 440  $\mu$ m/690 GHz band reveal new insights about the continuum and line emission of the region. The 440  $\mu$ m continuum flux density measurement from source *I* allows us to differentiate among the various proposed physical models: Source *I* can be well modeled by a “normal” protostellar SED consisting of a proton-electron free-free emission component at low frequencies and a strong dust component in the submillimeter bands. Furthermore, we find that the protostellar object SMA1 is clearly distinct from the hot core. The non-detection of SMA1 at cm and infrared wavelengths suggests that it may be one of the youngest sources in the entire Orion-KL region. The molecular line maps show emission mainly from the sources *I*, SMA1 and the hot core peak position. An analysis of the CH<sub>3</sub>CN(37<sub>K</sub> – 36<sub>K</sub>) *K*-ladder (*K* = 0...3) indicates a warm gas component of the order  $600 \pm 200$  K. In addition, we detect a large fraction ( $\sim 58\%$ ) of unidentified lines and discuss the difficulties of line identifications at these frequencies.

*Subject headings:* techniques: interferometric — stars: formation — ISM: individual (Orion-KL) — ISM: molecules — ISM: lines and bands — submillimeter

### 1. INTRODUCTION

The 440  $\mu$ m/690GHz band is almost entirely unexplored at high spatial resolution. In February 2005, the Submillimeter Array (SMA<sup>3</sup>) performed the first imaging campaign in that band with 6 antennas in operation, thus line and continuum imaging at  $1''$  resolution was possible at frequencies around 690 GHz. One of the early targets of this campaign was the Orion-KL region.

At a distance of  $\sim 450$  pc, Orion-KL is the closest and most studied region of massive star formation in our Galaxy. Furthermore, the Orion-KL hot core is known to be particularly rich in molecular line emission (e.g., Wright et al. 1996; Schilke et al. 2001; Beuther et al. 2005). The hot core as traced by (sub)millimeter dust continuum emission is a chain of clumps offset by  $\sim 1''$  from the radio source *I*. The hot core is rich in nitrogen-bearing molecules like CH<sub>3</sub>CN and NH<sub>3</sub> and has temperatures of the order of a few hundred Kelvin (e.g., Wilner et al. 1994; Wilson et al. 2000; Beuther et al. 2005). In contrast, the so-called compact ridge approximately  $5''$  to the south is particularly rich in CH<sub>3</sub>OH emission and has lower temperatures of the order 100 K (e.g., Wright et al. 1996; Liu et al. 2002; Beuther et al. 2005). In addition, the region harbors a complex cluster of infrared sources studied from near-to mid-infrared wavelengths (e.g., Dougados et al. 1993; Gezari et al. 1998; Greenhill et al. 2004; Shuping et al. 2004). At least two outflows are driven from the region, one high-velocity outflow in the south-east north-west direction (e.g., Allen & Burton 1993; Chernin & Wright 1996; Schultz et al. 1999), and one lower-velocity outflow in the north-east south-west direction (e.g., Genzel & Stutzki

1989; Blake et al. 1996; Chrysostomou et al. 1997; Stolovy et al. 1998; Beuther et al. 2005). The driving source(s) of the outflows are uncertain. Initial claims that it might be IRc2 are outdated now, and possible culprits are the radio source *I* and/or the infrared source *n*, also known as radio source *L* (Menten & Reid 1995).

In 2004, we observed Orion-KL at  $1''$  resolution with the SMA in the 865  $\mu$ m/348GHz band (Beuther et al. 2004, 2005). The molecular line data show a rich line forest resolving different spatial structures for the various species. The SiO(8–7) observations convincingly show that the north-east south-west outflow emission originates at source *I*. Temperature estimates based on a CH<sub>3</sub>OH multi-line fit result in values as high as 350 K for the hot core. In the 865  $\mu$ m submillimeter continuum data, source *I* was resolved from the hot core and source *n* was detected as well. The spectral energy distribution of source *I* from 8 to 348 GHz still allowed ambiguous interpretations of its physical nature (see also §3.1.3). Furthermore, a new continuum peak, SMA1, between sources *I* and *n* was detected; however, the nature of SMA1 was uncertain, as it could have been either an independent protostellar core or part of the extended hot core. In this paper, our new observations in the 440  $\mu$ m band clarify the nature of SMA1 and source *I*.

### 2. OBSERVATIONS

We observed Orion-KL with the SMA on February 19th, 2005, in the 440  $\mu$ m/690GHz band. Six antennas were equipped with 690 GHz receivers, and the covered baselines ranged between 16 and 68 m. The weather condi-

<sup>1</sup> Harvard-Smithsonian Center for Astrophysics, 60 Garden Street, Cambridge, MA 02138, USA

<sup>2</sup> Academia Sinica Institute of Astronomy and Astrophysics, National Taiwan University, No.1, Roosevelt Rd, Sec. 4, Taipei 106, Taiwan, R.O.C.

<sup>3</sup> The Submillimeter Array is a joint project between the Smithsonian Astrophysical Observatory and the Academia Sinica Institute of Astronomy and Astrophysics, and is funded by the Smithsonian Institution and the Academia Sinica.

tions were excellent with a zenith opacity, – measured with the NRAO tipping radiometer located at the Caltech Submillimeter Observatory –  $\tau(230\text{GHz})$  between 0.03 and 0.04 throughout the night. This corresponds to zenith opacities at 690 GHz between 0.6 and 0.8 ( $\tau(690\text{GHz}) \sim 20 \times (\tau(230\text{GHz}) - 0.01)$ , Masson 1994). The phase center was the nominal position of source *I* as given by Plambeck et al. (1995): R.A. [J2000]  $5^{\text{h}}35^{\text{m}}14.50^{\text{s}}$  and Dec. [J2000]  $-5^{\circ}22'30''.45$ . The FWHM of the primary beam of the SMA at these frequencies is  $18''$ , the aperture efficiency is  $\sim 0.4$ . For more details on the array and its capabilities see Ho et al. (2004), and recent updates are given at <http://sma1.sma.hawaii.edu/specs.html>.

The receivers operated in a double-sideband mode with an IF band of 4-6 GHz so that the upper and lower sidebands were separated by 10 GHz. The correlator had a bandwidth of 1.968 GHz and the channel spacing was 0.8125 MHz. The covered frequency ranges were 679.78 to 681.75 GHz and 689.78 to 691.75 GHz (Fig. 1). Bandpass calibration was done with observations of Callisto (angular diameter  $\sim 1.4''$ ). Since no quasar is strong enough in that band for calibration purposes, we calibrated phase and amplitude via frequent observations of Titan (angular diameter  $\sim 0.9''$ ). The distances of Callisto and Titan from Jupiter and Saturn were  $> 230''$  and  $\sim 190''$ , respectively. The contamination of the Callisto and Titan fluxes by their primaries is negligible due to mainly three reasons: (a) the primary beam pattern severely attenuates these planets since they are much more than 10 primary beams away, (b) the large size of the planets ( $40''$  for Jupiter,  $20''$  for Saturn) implies that a large fraction of their fluxes is resolved out, and (c) Due to the motion of the moons over the period of observations any small contamination will not be added coherently, further reducing the contamination issue.

The large angle between Titan and Orion-KL ( $\sim 40^\circ$ ) introduced larger than normal uncertainties in the phase and amplitude transfer. The flux calibration was performed with the Titan observations as well, for which a well-calibrated model has been created and used extensively at mm wavelengths (Gurwell & Muhleman 1995, 2000; Gurwell 2004). In the current observations, the upper sideband (USB) included the CO(6–5) line, which is quite broad as determined by using both observations of lower CO transitions and modeling of the expected line shape, assuming that CO has a uniform 50 ppm abundance in the Titan atmosphere (Gurwell 2004). Modeling the flux of the continuum LSB and continuum+CO(6–5) USB emission, the expected average Titan fluxes at the given dates were 12.0 and 22.3 Jy for the LSB and USB, respectively. Based on flux measurements of the two main continuum sources in Orion-KL using only the part of the spectra with no detectable line emission (§3.1), we estimate the relative flux accuracy between the upper and lower sideband to be better than 10%. The absolute flux calibration was estimated to be accurate within  $\sim 25\%$ .

Since Orion-KL is close to the celestial equator, and we have for most baselines only source data observed in an hour angle range from  $-2.6$  to  $+1.2$  hours (the data of only 3 baselines were usable over a longer range from  $-2.6$  to  $+4.5$  hours), imaging of the data proved to be difficult. Figure 2 shows the given uv-coverage and the resulting

dirty beam. In spite of the large-scale emission present in Orion-KL, we had to employ clean-boxes covering the central region around sources *I*, SMA1 and the main hot core peak to derive reasonable images because of the high side-lobe levels. Measured double-sideband system temperatures corrected to the top of the atmosphere were between 900 and 3500 K, depending on the elevation of the source. Our sensitivity was limited by the strong side-lobes of the strongest emission peaks, and thus varied between the continuum and the line maps of different molecules and molecular transitions. This limitation was mainly due to the incomplete sampling of short uv-spacings and the presence of extended structures. The achieved  $1\sigma$  rms of the  $440\mu\text{m}$  continuum image, produced by averaging the apparently line-free part of the USB spectrum (see §3.1), was  $\sim 700\text{ mJy/beam}$  – well above the expected  $1\sigma$  of  $\sim 41\text{ mJy/beam}$  for the given on-source time, the used bandpass and an average  $\tau(230\text{GHz}) = 0.037$  (corresponding to 0.61 mm precipitable water vapor). This larger rms was mainly due to the strong side-lobes and inadequate cleaning. The theoretical  $1\sigma$  rms per  $1\text{ km s}^{-1}$  channel was  $\sim 775\text{ mJy/beam}$ , whereas the measured  $1\sigma$  rms in  $1\text{ km s}^{-1}$  channel images was  $\sim 2.6\text{ Jy/beam}$ , again, because of the strong side-lobes and inadequate cleaning. The  $1\sigma$  rms for the velocity-integrated molecular line maps (the velocity ranges for the integrations were chosen for each line separately depending on the line-widths and intensities) ranged between 1.1 and 1.6 Jy/beam. The synthesized beams were  $1.4'' \times 0.9''$  using an intermediate weighting between natural and uniform (“robust” value 0 in MIRIAD). We calibrated the data within the IDL superset MIR developed for the Owens Valley Radio Observatory and adapted for the SMA (Scoville et al. 1993, see also the MIR cookbook by Charlie Qi at <http://cfa-www.harvard.edu/~cqi/micook.html>). The imaging was performed in MIRIAD (Sault et al. 1995).

### 3. RESULTS AND ANALYSIS

#### 3.1. $440\mu\text{m}$ continuum emission

The spectra presented in Figure 1 exhibit many molecular lines, therefore constructing a continuum image had to be done with great care. The continuum image presented in Fig. 3 (right panel) was constructed by averaging the part of the USB spectrum with no detectable line emission as shown in Fig. 1. The corresponding apparently line-free part of the LSB is considerably smaller and thus the comparable pseudo-continuum image noisier. Although we therefore omit the LSB data for the scientific interpretation, we point out that the peak fluxes in the LSB continuum image vary by less than 10% compared to the USB image. This shows the good relative flux calibration between both sidebands.

Weak lines below the detection limit may contribute to the continuum emission. To estimate the contamination from such weak lines, we produced an additional pseudo-continuum dataset of the lower sideband data including all spectral lines. We used the LSB data for this purpose because its line-contamination is more severe. Fitting two point-sources in the uv-domain (a) to the whole LSB continuum data and (b) to the apparently line-free LSB data (for details see §3.1.1), the measured fluxes from (a) were only  $\sim 15\%$  higher for source *I* and SMA1 than those from

(b). In our data, possible weak lines unidentified due to noise are on average less than 10% of the average peak-flux of the strong lines (Fig. 1). Since the strong lines already cover about half of the given bandpass (Fig. 1), the contribution from possible weak lines below the detection limit amounts to only about 1.5%. This is negligible compared to the absolute flux uncertainties.

The derived 440 $\mu$ m continuum emission map is shown in the right panel of Figure 3. To make a proper comparison with the 865 $\mu$ m emission, we also show the original image at that wavelength (Beuther et al. 2004), as well as an image of the 865 $\mu$ m observations using only the 30 to 160 k $\lambda$  data range, which is the range of baselines sampled by our 440 $\mu$ m data. In spite of strong side-lobes and the imaging problems described in §2, the 440 $\mu$ m map shows two distinct point-like sources associated with source *I* and SMA1. Comparing this image with the 30 to 160 k $\lambda$  image at 865 $\mu$ m, we find at the longer wavelength similar structures for source *I* and SMA1 plus emission from the hot core. Additional features like source *n* are not present in the 440 $\mu$ m continuum image, likely because of the poor imaging capabilities and thus strong side-lobes of the observations (see §2). The main difference between the 440 $\mu$ m and the 865 $\mu$ m continuum images is the strong presence of the hot core in the longer wavelength image, whereas we find only a small extension to the east at 440 $\mu$ m. Imaging of the spectral line data in the 440 $\mu$ m band (§3.2) shows that, in spite of the mentioned imaging limitations (§2), we can spatially image and separate line emission from source *I* and the hot core. Hence, while it remains puzzling that the typically strong hot core is only barely detectable in our 440 $\mu$ m image, it might be a real feature of the data indicating a peculiar low spectral index  $\alpha$  of the hot core emission (for a detailed discussion see §3.1.5).

### 3.1.1. Flux measurements

The 440 $\mu$ m continuum emission in Fig. 3 gives the impression that the point sources *I* and SMA1 are embedded in a larger-scale ridge emission. While Orion-KL is known to be part of the large-scale Orion molecular ridge (e.g., Lis et al. 1998), the larger-scale emission in our image is to some degree also an artifact of the data reduction, since we had to use clean boxes and thus shifted emission from the entire primary beam to the central region. Hence, flux measurements toward source *I* and SMA1 from the images will give values that are too high. To avoid these problems, we fitted the data in the uv-domain assuming:

- (a) two point sources at the positions of source *I* and SMA1;
- (b) two point sources at the positions of source *I* and SMA1 + an elliptical Gaussian;
- (c) three point sources at the positions of source *I*, SMA1, and the hot core peak position;
- (d) three point sources at the positions of source *I*, SMA1, and the hot core peak position + an elliptical Gaussian.

Afterwards, we imaged the models using exactly the same uv-coverage and imaging parameters employed previously for the real data. Figure 4 shows a direct comparison between the image of the original data and three model fits. We find that the models with additional larger-scale elliptical Gaussian component reproduce the data rather well.

Although the fitted fluxes for source *I* and SMA1 vary by less than 15% (within the calibration uncertainty) with or without the third point source at the position of the hot core, the three-point-sources+Gaussian model image most resembles the original data image. Therefore, we use this model for the following analysis.

These simplified models allow us to bracket the fluxes from sources *I*, SMA1 and the hot core. The three-point-source-only model likely overestimates the intrinsic fluxes because it adds some of the underlying large-scale emission to the point sources. Contrary to this, the three-point-source+Gaussian model underestimates the point-source contributions and thus the point-source fluxes. The measured values for both uv-fitting approaches are:

	3-point	3-point+Gaussian
$S(I)$	7.9 Jy	4.6 Jy
$S(\text{SMA1})$	7.1 Jy	3.5 Jy
$S(\text{HotCore(HC)})$	3.1 Jy	2.4 Jy
Gaussian		178 Jy (size 6.8'' $\times$ 2.7'')

Including the 25% calibration uncertainty, the 440 $\mu$ m fluxes measurements with conservative estimates of the error budget are:

$$3.5 < S(I) < 9.9 \Rightarrow S(I) \sim 6.7 \pm 3.2 \text{ Jy}$$

$$2.6 < S(\text{SMA1}) < 8.9 \Rightarrow S(\text{SMA1}) \sim 5.75 \pm 3.15 \text{ Jy}$$

$$1.8 < S(\text{HC}) < 3.9 \Rightarrow S(\text{HC}) \sim 2.85 \pm 1.05 \text{ Jy}$$

The errors are not to be understood as  $1\sigma$  or  $3\sigma$  values, but they rather give the extreme values of what the fluxes of the three sources could be. As outlined above, the line contamination of our continuum dataset is very low.

### 3.1.2. The large-scale structure

Obviously, from our data we cannot constrain well the large-scale flux distribution. However, the fitted 178 Jy are a lower limit to the large-scale flux since we have no data below 28 k $\lambda$ , and Johnstone & Bally (1999) measured a 450 $\mu$ m single-dish peak flux of 490 Jy with SCUBA at 7.5''. Furthermore, we investigated the influence of a large source with a flux of a few hundred Jy on our observations. Modeling different source sizes and *observing* them with the given uv-coverage, the size-scale of the large-scale emission has to exceed 11''. Larger sources are filtered out by the observations and do not distort the observed continuum image significantly, whereas smaller sources with large flux would completely dominate the observations. The scale of 11'' corresponds approximately to the size-scales theoretically traceable by the shortest baselines of 28 k $\lambda$  (corresponding to approximately 9'' scales).

### 3.1.3. Source *I*

Prior to these observations, the SED of source *I* could be fitted well by two very different models, either as the result of optically thick proton-electron free-free emission up to 100 GHz plus dust emission that accounts for most of the submm flux, or  $\text{H}^-$  free-free emission that gives rise to a power-law spectrum with a power-law index of  $\sim 1.6$  (Beuther et al. 2004). Since the two models vary strongly at higher frequencies, an accurate 440 $\mu$ m continuum flux measurement was of utmost importance in discriminating between these models.

Figure 5 shows the complete SED of source *I* from 8 to 690 GHz. The measured 690 GHz flux fits the model of a proton-electron free-free plus dust emission spectrum well, but not the model of the power-law spectrum expected for  $H^-$  free-free emission. Therefore, the 440  $\mu\text{m}$  continuum data can discriminate between the two models, and the SED of source *I* turns out to be a rather typical SED for deeply embedded protostellar sources. The important result here is that the turn-over frequency (i.e., the transition from optically thick to optically thin emission) is much higher in source *I* than in other protostars where it is typically in the range of 10 to 40 GHz.

### 3.1.4. SMA1

The observations show that SMA1 is not just an extension of the hot core, but is an independent protostellar source. Based on PdBI  $\text{HC}_3\text{N}(10-9)$  observations of vibrational excited lines, de Vicente et al. (2002) predicted an additional massive protostellar source in the region approximately 1.8'' south of source *I*, which is the location of SMA1. Only two flux measurements exist for SMA1: at 865  $\mu\text{m}$  ( $S \sim 0.36 \pm 0.07$  Jy, Beuther et al. 2004) and at 440  $\mu\text{m}$  ( $S \sim 5.75 \pm 3.15$  Jy). The spectral index between these two bands is  $S \propto \nu^\alpha$  with  $\alpha \sim 4.0^{+0.9}_{-1.4}$ . In spite of the broad range of potential  $\alpha$ , the data are consistent with a typical dust opacity index  $\beta = \alpha - 2$  in star-forming regions of 2. The non-detection of SMA1 at cm and infrared wavelengths suggests that it may be one of the youngest sources of the evolving cluster.

### 3.1.5. The Hot Core

The hot core flux values we derived above are probably more uncertain than those from source *I* and SMA1 because the hot core is only weakly discernible from the rest of the image in the original data as well as the model. Furthermore, the response of the continuum and line emission to the poor uv-sampling is not the same in interferometric studies, and we cannot entirely exclude that the weakness of the hot core in the 440  $\mu\text{m}$  data is caused by this poor uv-sampling and the resulting imaging problems. Keeping in mind these uncertainties, we nevertheless can use the existing data to estimate a spectral index between the previous 865  $\mu\text{m}$  measurement and this new data. The flux measurements in the two bands toward the hot core peak position ( $S(865\mu\text{m}) \sim 0.54 \pm 0.11$  Jy, Beuther et al. 2004, and  $S(440\mu\text{m}) \sim 2.85 \pm 1.05$  Jy) result in a range of potential spectral indices  $S \propto \nu^\alpha$  with  $\alpha \sim 2.4^{+0.8}_{-0.9}$ . These values are considerably lower than for source *I* and SMA1.

Single-dish spectral index studies toward the Orion A molecular cloud qualitatively find a somewhat lower spectral index toward Orion-KL than toward most of the rest of the Orion A molecular cloud (Lis et al. 1998; Johnstone & Bally 1999), but the two studies do not agree quantitatively. Lis et al. (1998) find a dust opacity index  $\beta \sim 1.8$  corresponding in the Rayleigh-Jeans limit to a spectral index  $\alpha \sim 3.8$ , whereas Johnstone & Bally (1999) find a spectral index  $\alpha \sim 2.2$ . Nevertheless, considering the large number of potential uncertainties (e.g., calibration, different beam sizes, line contamination, etc.), the qualitatively lower spectral index  $\alpha$  toward Orion-KL compared with its surroundings appears a reliable result from the single-dish studies.

In contrast to source *I* and SMA1, where the spectral indices are both consistent with typical values of  $\alpha$  around 4 in star-forming regions, the lower spectral index toward the hot core is intriguing. Furthermore, lower-resolution observations show that on larger spatial scales the data are dominated by the apparently more extended hot core emission (e.g., Plambeck et al. 1995; Blake et al. 1996; Beuther et al. 2004). Therefore, the different spectral indices indicate that the lower single-dish spectral index may be due to hot core emission distributed over larger spatial scales, whereas the protostellar sources *I* and SMA1 exhibit spectral indices more typical of those from other star-forming regions.

## 3.2. Spectral line emission

We detected 24 spectral lines over the entire bandpass of 4 GHz (Fig. 1 & Table 1). This is a significantly lower line number than the  $\sim 150$  lines over the same spectral width at 348 GHz. The lower sensitivity of the 690 GHz data compared with the 345 GHz observations accounts for this difference to some degree. Furthermore, at 690 GHz each line of a given  $\Delta\nu$  covers twice the frequency range than at 345 GHz, and thus strong lines dominate a broader part of the spectrum than at lower frequencies. Furthermore, to first order the observing frequency is proportional to the average energy levels of observable lines in that frequency range, and the lower number of line detections at 690 GHz indicates that the bulk of the gas is at lower temperatures (see temperature discussion in §3.3). Nevertheless, the energy levels of the 690 GHz lines (Table 1) show that a very warm gas component has to be present in the region as well. Temperature estimates based on the  $\text{CH}_3\text{CN}(37_K - 36_K)$  are derived below (§3.3). Comparing these spectra with the single-dish spectra toward the same region (Schilke et al. 2001; Harris et al. 1995), we find a large number of lines previously not detected in this region. Line identifications were done first using the line survey by Schilke et al. (2001), and then cross-checking the identifications with the molecular databases at JPL and CDMS (Poynter & Pickett 1985; Müller et al. 2001). It has to be noted that the unambiguous identification of spectral lines becomes more difficult at higher frequencies, which is discussed in §3.4.

Table 1 also shows the line-widths derived from Gaussian fits to the vector-averaged spectra on a short baseline of 25 m (Fig. 1). Since the measured line-widths are associated with gas from the whole emission in the primary beam, they do not represent the line-width toward a selected position but rather an average over the whole region. The derived values for  $\Delta\nu$  range between 4.8 and 16.4  $\text{km s}^{-1}$ . We could not fit the  $\text{CO}(6-5)$  line due to the missing flux. While some of the broader line-widths may be due to the outflows in the region, this is probably not the main reason for most of the lines since the spectra often resemble a Gaussian profile. It seems more likely that different velocity components as well as large intrinsic line-widths toward each position due to turbulence and/or internal motion cause a reasonable fraction of the line-width. For a discussion of the  $\text{CH}_3\text{CN}$  line-widths, see §3.3.

Figure 6 presents the images of the velocity-integrated emission of a few of the identified molecular lines in

the bandpass. As discussed in §2 and §3.1, imaging of the emission turns out to be difficult, as evidenced by the strong negative side-lobes in Fig. 6. Since our primary beam is rather small (18'') and the imaging gets worse towards the edge of the primary beam, we consider only emission at the centers of the maps to be reliable. All line images in Fig. 6 show considerable emission toward source *I*, SMA1 and the hot core peak position. C<sup>33</sup>S(14–13) peaks toward SMA1 with lower level emission from the hot core and source *I*. In contrast to this, the line images from CH<sub>3</sub>CN(37<sub>2</sub>–36<sub>2</sub>), CH<sub>3</sub>OH(22<sub>1</sub>–21<sub>2</sub>) and SO<sub>2</sub>(35<sub>3,33</sub> – 34<sub>2,32</sub>) all show emission peaks from source *I*, SMA1 and the hot core peak position. The HNC(31<sub>2,29</sub> – 30<sub>2,28</sub>) image exhibits emission peaks associated with source *I* and SMA1, and only lower-level emission from the hot core position. A striking difference between this 440  $\mu$ m line images and our previous study in the 865  $\mu$ m band (Beuther et al. 2005) is that the higher excited lines in the 440  $\mu$ m band show line emission from source *I*. In the 865  $\mu$ m band, we found mainly SiO emission from source *I*, other species appear to avoid the source in the lower frequency band. This indicates the presence of high temperatures in the close environment of source *I*.

We could not produce reliable emission maps for the CO(6–5) and H<sup>13</sup>CN(8–7) lines. While this is less of a surprise for CO, which is known to be extended and thus difficult to image interferometrically, H<sup>13</sup>CN was expected to be far more compact, comparable to many of the other imaged lines. However, comparing all lines in our frequency setup (excluding only the CO(6–5) line), the H<sup>13</sup>CN(8–7) line has one of the broadest linewidths ( $\Delta v \sim 16.2$  km s<sup>−1</sup>), and thus may be more strongly affected by the molecular outflows present than initially expected. This could explain our inability to properly image the H<sup>13</sup>CN(8–7) emission.

### 3.3. CH<sub>3</sub>CN(37<sub>K</sub> – 36<sub>K</sub>): temperature estimates and line-widths

Since we observed the  $K = 0, 1, 2, 3$  lines of the CH<sub>3</sub>CN(37<sub>K</sub> – 36<sub>K</sub>) lines (the  $K = 0, 1$  lines are blended), we can use this  $K$ -series for temperature estimates of the warm gas component in the regions. Figures 6 & 7 show the integrated CH<sub>3</sub>CN(37<sub>2</sub> – 36<sub>2</sub>) emission map and spectra of all  $K$ -components toward the CH<sub>3</sub>CN peak positions associated with source *I*, SMA1, and the hot core.

Using the XCLASS superset to the CLASS software (Peter Schilke, priv. comm.), we produced model spectra in local thermodynamic equilibrium (Fig. 7). This software package uses the line catalogs from JPL and CDMS (Poynter & Pickett 1985; Müller et al. 2001). Because the  $K = 3$  component has double the statistical weight than the  $K = 0, 1, 2$  lines, one expects in the optical thin case larger line intensities for the  $K = 3$  transition. The optically thin model spectra reproduce the relative line intensities well toward SMA1 and the hot core. Toward source *I*, the modeled  $K = 3$  intensity is a bit larger than observed indicating increasing optical depth there. The upper energy levels  $E_u$  of the various K-ladder lines range only between 621 and 685 K (Table 1), and the data are not very sensitive to the temperature. We find reasonable model spectra in the 600 K regime with a large potential range of temperatures of  $\pm 200$  K. The CH<sub>3</sub>CN

model column densities we used are of the order a few times 10<sup>15</sup> cm<sup>−2</sup>, and the line-width adopted for the modeling was 6.5 km s<sup>−1</sup>. In spite of the large errorbars, the temperatures traced by these high-energy lines are, as expected, higher than the highest temperatures of 350 K previously derived from our CH<sub>3</sub>OH multi-line analysis in the 865  $\mu$ m band (Beuther et al. 2005). We attribute this temperature difference mainly to the various gas components at different temperatures and densities, and to the different excitation energies of the spectral lines in the 690 and 337 GHz bands.

Furthermore, we can compare the modeled CH<sub>3</sub>CN(37<sub>K</sub> – 36<sub>K</sub>) line-widths of the order 6.5 km s<sup>−1</sup> with the previous SMA observations of the CH<sub>3</sub>CN(19<sub>8</sub> – 18<sub>8</sub>) line at 348 GHz (Beuther et al. 2005). The measured CH<sub>3</sub>CN(19<sub>8</sub> – 18<sub>8</sub>) from SMA1 and the hot core are 4.6 and 4.1 km s<sup>−1</sup>, respectively. Beuther et al. (2005) found only very weak CH<sub>3</sub>CN(19<sub>8</sub> – 18<sub>8</sub>) toward source *I*. Although the excitation temperatures  $E_u$  of the CH<sub>3</sub>CN(37<sub>2</sub> – 36<sub>2</sub>) and the CH<sub>3</sub>CN(19<sub>8</sub> – 18<sub>8</sub>) lines are approximately the same (649 and 624 K, respectively), it is interesting that the line-width toward the CH<sub>3</sub>CN(37<sub>2</sub> – 36<sub>2</sub>) is larger. Since the critical densities between the CH<sub>3</sub>CN(37<sub>K</sub> – 36<sub>K</sub>) and CH<sub>3</sub>CN(19<sub>K</sub> – 18<sub>K</sub>) series vary by about one order of magnitude ( $\sim 10^8$  and  $\sim 10^7$  cm<sup>−3</sup>, respectively), this indicates that the higher density gas CH<sub>3</sub>CN(37<sub>K</sub> – 36<sub>K</sub>) lines are likely subject to significantly more turbulent motions. As already pointed out by Sutton et al. (1986), radiative excitation is unlikely to significantly affect the populations of the vibrational ground state transitions, even for high J-levels.

### 3.4. Unidentified lines (UL)

Fourteen out of the 24 detected spectral lines remain unidentified or only tentatively identified. Such a high percentage of unidentified lines ( $\sim 58\%$ ) has rarely been reported, to our knowledge only recently toward SgrB2 (Friedel et al. 2004). The previous single-dish line surveys of Orion-KL report percentages of unidentified lines between 8 and 15% (Schilke et al. 1997, 2001; Comito et al. 2005). Orion-KL is known to have a number of different velocity components approximately between 2 and 9 km s<sup>−1</sup> (e.g., Genzel & Stutzki 1989), and we cannot determine at which velocity an unidentified line is beforehand. Hence, at 690 GHz the frequency range of potential molecular lines between 2 and 9 km s<sup>−1</sup> is 16 MHz, compared to 8 MHz at 345 GHz ( $\Delta\nu = \Delta v \times \nu/c$ ). Furthermore, going to higher frequencies, astronomical spectral line studies are rare and identifications that rely only on laboratory work are difficult. Hence, identifying spectral lines gets more complicated at higher frequencies.

Figure 8 presents some of the integrated line emission maps of the ULs. Since these lines are on average of lower intensity, the signal-to-noise ratio in the maps is worse than for the identified lines in Fig. 6. The rest-frequencies listed for the ULs in Table 1 (and shown in Fig. 8) correspond to the lines being set to a  $v_{lsr}$  of 5 km s<sup>−1</sup>, implying the potential range of frequencies for each line as discussed above. In principle, it should sometimes be possible to associate unidentified lines with molecular families (e.g., oxygen-, nitrogen-, or sulphur-bearing species) based on the spatial distribution of the gas (see, e.g., the previous

865  $\mu\text{m}$  Orion line studies by Beuther et al. 2005). However, since the quality of the images is rather poor, this is a difficult task for this dataset. Nevertheless, we tried to associate some unidentified lines with potential molecular transitions. Table 1 lists a few tentative candidate lines for the ULs, which, however, are only suggestions and not real identifications.

#### 4. DISCUSSION AND CONCLUSIONS

The presented line and continuum data of Orion-KL in the 440  $\mu\text{m}$ /690GHz band show the power of high-spatial-resolution studies in the submm wavelength bands. The measured continuum flux from source *I* allows us to differentiate between various previously proposed physical models: Source *I* appears to be a rather “normal” protostellar object with a SED fitted by a two-component model of proton-electron free-free emission below 100 GHz plus a dust component contributing to the flux in the submm bands. Furthermore, the source SMA1 becomes more prominent at higher frequencies and is clearly distinguishable from the hot core emission. Since SMA1 is detected neither at cm nor at infrared wavelengths, it may be one of the youngest sources of the evolving cluster. The only weak detection of the hot core at 440  $\mu\text{m}$  is puzzling. Although it might be a real feature of the new high-spatial-resolution 440  $\mu\text{m}$  continuum data, we cannot

entirely exclude that it is caused by the poor uv-sampling and resulting imaging problems. Keeping the uncertainties in mind, we find a lower spectral index toward the hot core compared with source *I* and SMA1. This is consistent with lower spectral indices found toward Orion-KL in lower-spatial-resolution single-dish observations that are dominated by the hot core emission.

The spectral line maps trace a warm gas component at the center of the region, mainly confined to the sources *I*, SMA1 and the hot core peak position. Temperature estimates based on the  $\text{CH}_3\text{CN}(37_K - 36_K)$  K-ladder ( $K = 0..3$ ) lines indicate a warm gas component in the regime of  $600 \pm 200$  K. The number of unidentified lines in the given setup is large. Potential reasons are discussed, of which the two main ones are likely the large potential spread in velocity, and thus frequency, of the ULs, and the less explored submm wavelength band.

We would like to thank Peter Schilke for providing the XCLASS software to model the  $\text{CH}_3\text{CN}$  spectra. Thanks very much also to Darek Lis for discussing spectral indices in Orion-KL. We also appreciate the helpful comments from the referee. H.B. acknowledges financial support by the Emmy-Noether-Program of the Deutsche Forschungsgemeinschaft (DFG, grant BE2578/1).

#### REFERENCES

- Allen, D. A. & Burton, M. G. 1993, *Nature*, 363, 54  
 Beuther, H., Zhang, Q., Greenhill, L. J., et al. 2004, *ApJ*, 616, L31  
 —. 2005, *ApJ* in press  
 Blake, G. A., Mundy, L. G., Carlstrom, J. E., et al. 1996, *ApJ*, 472, L49  
 Chernin, L. M. & Wright, M. C. H. 1996, *ApJ*, 467, 676  
 Chrysostomou, A., Burton, M. G., Axon, D. J., et al. 1997, *MNRAS*, 289, 605  
 Comito, C., Schilke, P., Phillips, T. G., et al. 2005, *ApJS*, 156, 127  
 de Vicente, P., Martín-Pintado, J., Neri, R., & Rodríguez-Franco, A. 2002, *ApJ*, 574, L163  
 Dougados, C., Lena, P., Ridgway, S. T., Christou, J. C., & Probst, R. G. 1993, *ApJ*, 406, 112  
 Friedel, D. N., Snyder, L. E., Turner, B. E., & Remijan, A. 2004, *ApJ*, 600, 234  
 Genzel, R. & Stutzki, J. 1989, *ARA&A*, 27, 41  
 Gezari, D. Y., Backman, D. E., & Werner, M. W. 1998, *ApJ*, 509, 283  
 Greenhill, L. J., Gezari, D. Y., Danchi, W. C., et al. 2004, *ApJ*, 605, L57  
 Gurwell, M. A. 2004, *ApJ*, 616, L7  
 Gurwell, M. A. & Muhleman, D. O. 1995, *Icarus*, 117, 375  
 —. 2000, *Icarus*, 145, 653  
 Harris, A. I., Avery, L. W., Schuster, K.-F., Tacconi, L. J., & Genzel, R. 1995, *ApJ*, 446, L85  
 Ho, P. T. P., Moran, J. M., & Lo, K. Y. 2004, *ApJ*, 616, L1  
 Johnstone, D. & Bally, J. 1999, *ApJ*, 510, L49  
 Lis, D. C., Serabyn, E., Keene, J., et al. 1998, *ApJ*, 509, 299  
 Liu, S., Girart, J. M., Remijan, A., & Snyder, L. E. 2002, *ApJ*, 576, 255  
 Müller, H. S. P., Thorwirth, S., Roth, D. A., & Winnewisser, G. 2001, *A&A*, 370, L49  
 Masson, C. R. 1994, in *Astronomical Society of the Pacific Conference Series*, 87  
 Menten, K. M. & Reid, M. J. 1995, *ApJ*, 445, L157  
 Plambeck, R. L., Wright, M. C. H., Mundy, L. G., & Looney, L. W. 1995, *ApJ*, 455, L189  
 Poynter, R. L. & Pickett, H. M. 1985, *Appl. Opt.*, 24, 2235  
 Sault, R. J., Teuben, P. J., & Wright, M. C. H. 1995, in *ASP Conf. Ser. 77: Astronomical Data Analysis Software and Systems IV*, 433  
 Schilke, P., Benford, D. J., Hunter, T. R., Lis, D. C., & Phillips, T. G. 2001, *ApJS*, 132, 281  
 Schilke, P., Groesbeck, T. D., Blake, G. A., & Phillips, T. G. 1997, *ApJS*, 108, 301  
 Schultz, A. S. B., Colgan, S. W. J., Erickson, E. F., et al. 1999, *ApJ*, 511, 282  
 Scoville, N. Z., Carlstrom, J. E., Chandler, C. J., et al. 1993, *PASP*, 105, 1482  
 Shuping, R. Y., Morris, M., & Bally, J. 2004, *AJ*, 128, 363  
 Stolovy, S. R., Burton, M. G., Erickson, E. F., et al. 1998, *ApJ*, 492, L151  
 Sutton, E. C., Blake, G. A., Genzel, R., Masson, C. R., & Phillips, T. G. 1986, *ApJ*, 311, 921  
 Wilner, D. J., Wright, M. C. H., & Plambeck, R. L. 1994, *ApJ*, 422, 642  
 Wilson, T. L., Gaume, R. A., Gensheimer, P., & Johnston, K. J. 2000, *ApJ*, 538, 665  
 Wright, M. C. H., Plambeck, R. L., & Wilner, D. J. 1996, *ApJ*, 469, 216

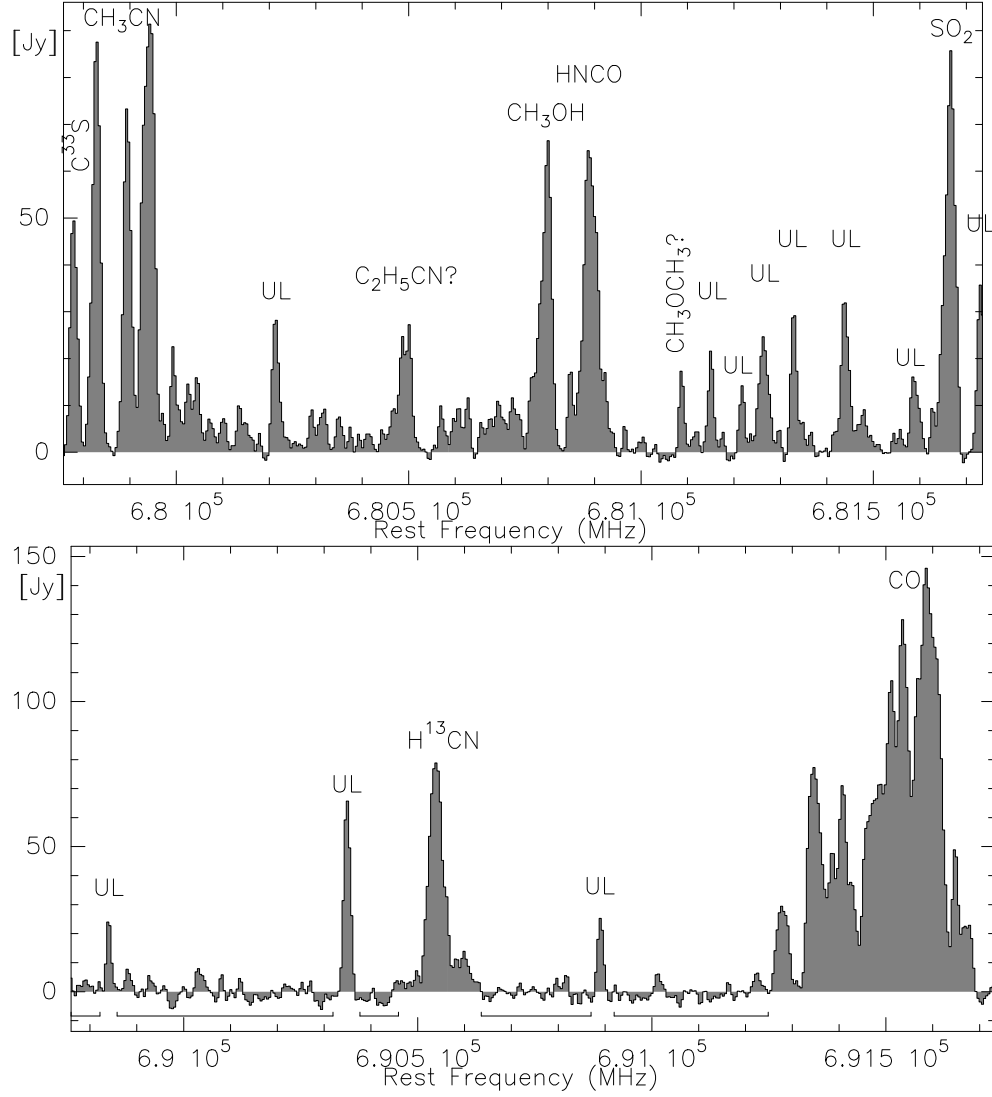


FIG. 1.— Vector-averaged lower and upper sideband spectra in the uv-domain on a baseline of  $\sim 25$  m. The data are averaged over an hour angle range from  $-2.6$  to  $+4.5$  hours with a total on-source integration time of 176 minutes. UL marks unidentified lines and “?” marks tentatively identified lines. The lines at the bottom of the USB spectrum mark the apparently line-free part of the spectrum, which we used to produce the 440  $\mu$ m continuum image (Figs. 3 & 4).

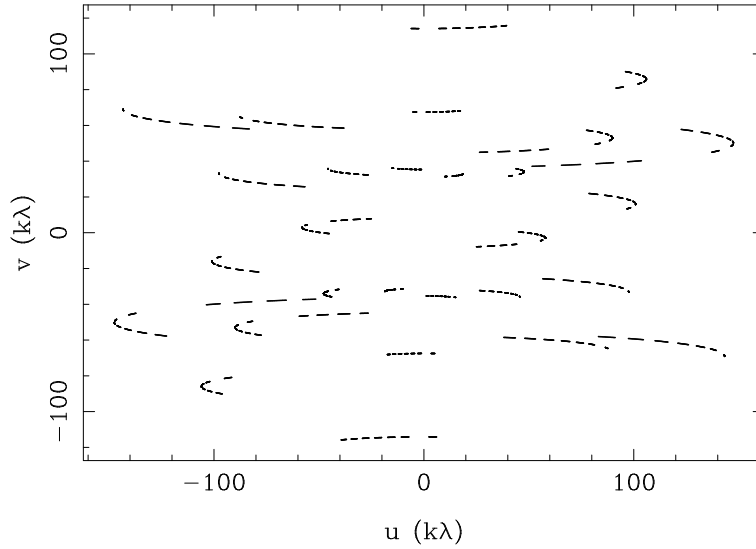


FIG. 2.— The top panel shows the uv-coverage of the observations. The bottom panel presents the resulting dirty beam, contour levels cover the range  $\pm 1$ , in steps of  $\pm 0.125$ .

FIG. 3.— Submillimeter continuum images of Orion-KL. Positive emission is always shown in gray scale with contours, negative features – due to missing short spacings and the calibration/imaging difficulties discussed in §2 – are presented in dashed contours. The **left** panel shows the previously published 348 GHz continuum data (Beuther et al. 2004). The contours start at the  $2\sigma$  level of  $70 \text{ mJy beam}^{-1}$  and continue in  $2\sigma$  steps. The main sources in the region are labeled by name. The **middle** panel shows an image of the same region, with a limited range of uv-data between 30 and 160  $k\lambda$ . The contouring is the same as in the left panel, and the stars mark the four sources identified in the left panel. The **right** panel shows the new 690 GHz continuum data covering a uv-range between 30 and 160  $k\lambda$  again (blanking the only bin below 30  $k\lambda$  at 28  $k\lambda$ ). The contouring is done in 10 to 90% steps from the peak emission of 10.3 Jy, and the stars again mark the sources identified in the left panel. The synthesized beams are presented at the bottom-left of the panels. The different synthesized beams in the middle and right panel result from a different uv-sampling, although we applied the same uv-limits.

FIG. 4.— Original image and model-fits to the 690 GHz continuum data. **1.)** Original image, **2.)** 2 point source model, **3.)** 2 point source + Gaussian model, and **4.)** 3 point source + Gaussian model. The contouring is done in  $\pm 10$  to  $\pm 90\%$  steps from the peak emission of the three images. The peak values are 10.3, 7.7, 10.2 and 10.6 Jy for panels 1 to 4, respectively. The stars again mark the sources identified in the left panel of Figure 3. The synthesized beams are presented at the bottom-left of each panel.



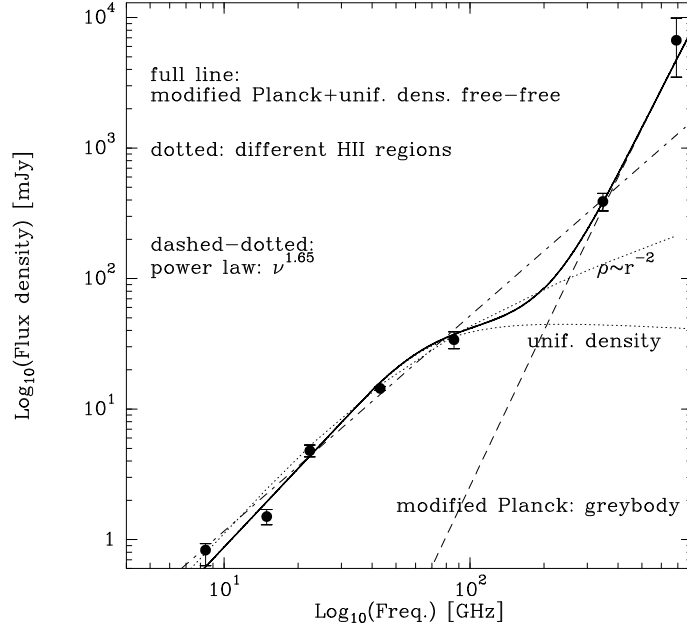


FIG. 5.— The SED of source *I*. The measured fluxes are labeled as filled circles with error bars, and the various lines show different attempts to fit the data as labeled within the plot. The 15, 22 and 86 GHz fluxes are taken from Plambeck et al. (1995) and references therein, the 8 and 43 GHz measurements are more recent values (consistent with the error bars of the previous measurements by Menten & Reid (1995), M.J. Reid et al. in prep.), the 345 GHz data point is from Beuther et al. (2004), and the 690 GHz point is from this work.

FIG. 6.— Integrated line emission maps after continuum subtraction: The top-left panel shows for comparison again the continuum image as presented in Fig. 3, and the other 5 panels show representative molecular line maps as labeled within each panel. Positive emission is presented in gray scale and full contours, and negative emission – due to missing short spacings – is shown in dashed contours. The contours always range from 10 to 90% of the peak emission in each image. The synthesized beams are shown at the bottom-left of each panel.

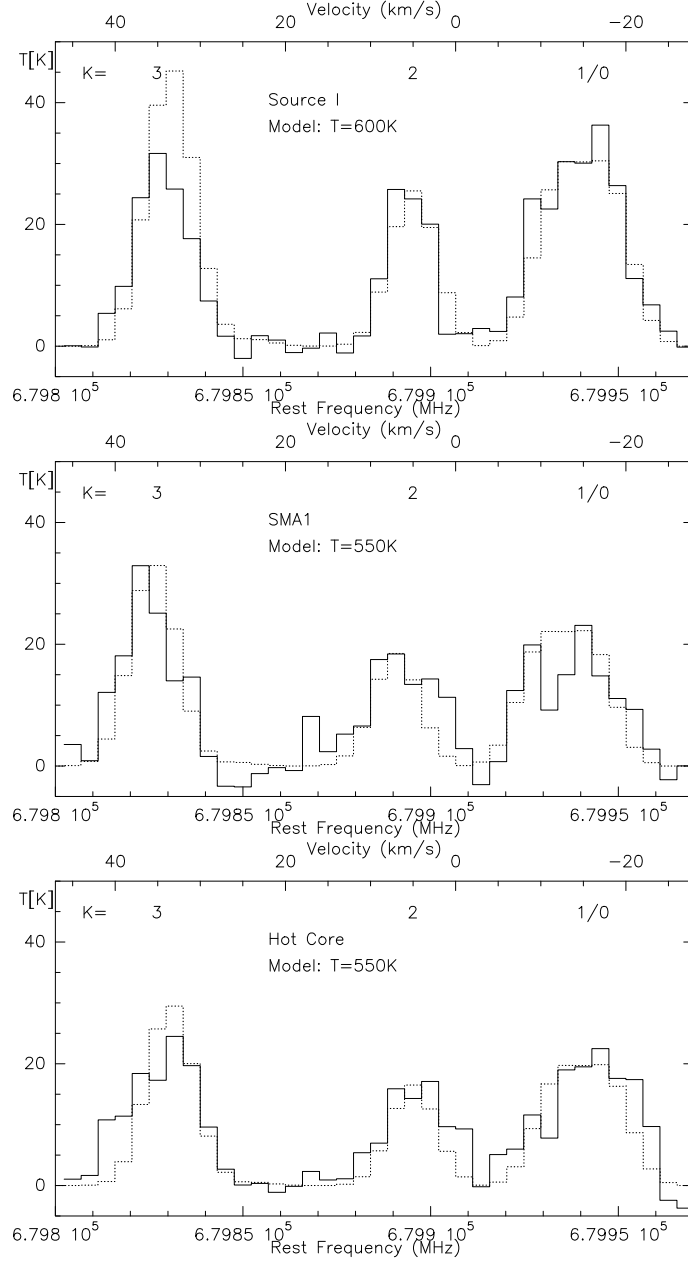


FIG. 7.—  $\text{CH}_3\text{CN}(37_K - 36_K)$  spectra taken toward the  $\text{CH}_3\text{CN}$  peak positions associated with source *I*, SMA1 and the hot core (see Fig. 6). The full lines show the data, and the dotted lines LTE model spectra (adopted temperatures are given in each panel). The data are not very sensitive to the temperatures and can be modeled with  $T$  varying approximately  $\pm 200$  K.

FIG. 8.— Integrated line emission maps of some unidentified lines after continuum subtraction: positive emission is presented in gray scale and full contours, and negative emission – due to missing short spacings – is shown in dashed contours. The contours always range from 10 to 90% of the peak emission in each image. The rest-frequency for each line set to a  $v_{\text{LSR}} = 5 \text{ km s}^{-1}$  is shown at the top-left of each map. The symbols are the same as in the previous Figures, and the synthesized beams are shown at the bottom-left of each panel.

TABLE 1  
OBSERVED LINES

$\nu^a$ [GHz]	line	$E_u$ [K]	$\Delta v^b$ [km s $^{-1}$ ]	Tentative? $^c$
679.781	C $^{33}$ S(14–13)	247	7.1	
679.831	CH $_3$ CN(37 $_3$ – 36 $_3$ )	688	8.3	
679.895	CH $_3$ CN(37 $_2$ – 36 $_2$ )	649	8.3	
679.934	CH $_3$ CN(37 $_1$ – 36 $_1$ )	628	13.4 $^f$	
679.947	CH $_3$ CN(37 $_0$ – 36 $_0$ )	621	13.4 $^f$	
680.210	UL $^d$		7.1	C $_2$ H $_3$ CN(72 $_{4,69}$ – 71 $_{4,68}$ )@680.211 OCS(56 – 55)@680.213
680.485	UL		13.8 $^f$	C $_2$ H $_5$ CN(78 $_{4,75}$ – 77 $_{4,74}$ )@680.481
680.500	UL		13.8 $^f$	C $_2$ H $_5$ CN(78 $_{3,75}$ – 77 $_{3,74}$ )@680.507
680.804	CH $_3$ OH(22 $_1$ – 21 $_2$ )A $^-$	606	12.6	
680.890	HNCO(31 $_{2,29}$ – 30 $_{2,28}$ )	696	16.4	
681.086	UL		4.8	CH $_3$ CN(37 $_7$ – 36 $_7$ ) $v_8$ = 1@681.087 CH $_3$ OCH $_3$ (19 $_{6,13}$ – 18 $_{5,14}$ )@681.090
681.150	UL		5.5	C $_2$ H $_5$ OH(56 $_{21,35}$ – 56 $_{21,35}$ )@681.152
681.218	UL		5.2	CH $_3$ CN(37 $_9$ – 36 $_9$ ) $v_8$ = 2@681.216 C $_2$ H $_5$ CN(70 $_{8,63}$ – 71 $_{3,68}$ )@681.224
681.263	UL		10.4	HCOOCH $_3$ (35 $_{8,28}$ – 35 $_{4,31}$ )@681.265 SO $_2$ (68 $_{9,59}$ – 68 $_{8,60}$ )@681.266 $^{33}$ SO(16 – 15)@681.269
681.328	UL		6.3	CH $_3$ CN(37 $_1$ – 36 $_1$ ) $v_8$ = 2@681.329
681.440	UL		8.6	CH $_3$ CN(37 $_5$ – 36 $_5$ ) $v_8$ = 1@681.438
681.589	UL		8.7	CH $_3$ CN(37 $_7$ – 36 $_7$ ) $v_8$ = 2@681.590
681.674	SO $_2$ (35 $_{3,33}$ – 34 $_{2,32}$ )	598	11.4	
681.733 $^e$	UL			
689.840	UL		5.2	D $_2$ CO(20 $_{2,18}$ – 20 $_{2,19}$ )@689.840 C $_2$ H $_3$ CN(21 $_{6,15}$ – 22 $_{4,18}$ )@689.842 SiN(16 – 15)@689.842 C $_2$ H $_5$ CN(28 $_{10,19}$ – 27 $_{9,18}$ )@689.842
690.349	UL		7.0	
690.551	H $^{13}$ CN(8–7)	149	16.2	
690.890	UL		6.0	HCOOCH $_3$ (27 $_{7,21}$ – 26 $_{6,20}$ )@690.891 C $_2$ H $_3$ CN(72 $_{30,42}$ – 71 $_{30,41}$ )@690.892 C $_2$ H $_5$ CN(23 $_{11,12}$ – 22 $_{10,13}$ )@690.892
691.473	CO(6–5)	116	? $^g$	

$^a$ The frequency uncertainties are below 1 MHz, mostly even below 0.1 MHz. The frequencies for the ULs are derived via setting the  $v_{lsr}$  to 5 km s $^{-1}$ .

$^b$ FWHM of Gaussian fits to the vector-averaged spectra of the short 25 m baseline (see Fig. 1).

$^c$ Tentative molecular transition identifications which are still very uncertain!

$^d$ UL: Unidentified line.

$^e$ This line is at the edge of the bandpass and thus only partly detected. Therefore, the frequency is even more uncertain.

$^f$ Line blend.

$^g$ Due to missing flux, a line fit does not make sense.

This figure "f2b.jpg" is available in "jpg" format from:

<http://arXiv.org/ps/astro-ph/0509771v1>

This figure "f3.jpg" is available in "jpg" format from:

<http://arXiv.org/ps/astro-ph/0509771v1>

This figure "f4.jpg" is available in "jpg" format from:

<http://arXiv.org/ps/astro-ph/0509771v1>

This figure "f6.jpg" is available in "jpg" format from:

<http://arXiv.org/ps/astro-ph/0509771v1>

This figure "f8.jpg" is available in "jpg" format from:

<http://arXiv.org/ps/astro-ph/0509771v1>